Harnessing Buckling to Design Architected Materials that Exhibit Effective Negative Swelling

*Jia Liu, Tianyu Gu, Sicong Shan, Sung H. Kang, James C. Weaver, and Katia Bertoldi**

Inspired by the need to develop materials capable of targeted and extreme volume changes during operation, we combine numerical simulations and experiments to design a new class of soft architected materials that effectively exhibit a negative swelling behavior. The proposed system consists of an array of identical layered plates composed of common soft materials that swell when imbibing a solvent. Our results reveal that, by designing the individual plates so that they buckle into a half sinusoid during the swelling process, a net reduction of projected surface area coverage is achieved. The proposed concept expands the abilities of existing soft materials and structures and demonstrates a robust route to further control their volume in a highly tunable manner.

Soft materials such as elastomers and gels can swell up to 1000-fold when immersed in a solvent,[1–4] thus enabling the design of soft switches[5,6] and actuators.[7–11] Moreover, soft materials whose swelling is affected by changes in temperature,[12] pH,[13] ionic concentration,[14] and electricity[15] have been incorporated into a wide range of enviromentally responsive devices, including microfluidic valves,[16–18] sensors,[19–24] and artificial muscles.[25–28] However, despite intensive efforts to control and tune their swellability, this behavior has primarily been used as a means to increase the volume of a material or device of interest. In contrast, negative swelling (i.e., the ability to achieve volumes smaller than that of the dry state) is a comparatively rare phenomenon[29] and no strategy has been reported to achieve negative volume changes in composite structures made of common swellable soft materials.

Here, inspired by the fact that effective negative thermal expansion can be achieved in structures where the overall expansion is compensated by internal bending deformation[30–32] and that buckling can trigger large bending deformation, we exploit mechanical instabilities to design a new class of 2D architected materials with effective negative swelling ratio. In our proposed system, the constituent building block consists of a plate sandwiched between two thin layers (see **Figure 1**a), all fabricated out of common soft materials that swell when immersed in a solvent, but with different stiffness and swelling characteristics. While an homogeneous plate that imbibes a solvent expands in all directions, such a heterogeneous layered plate buckles and adopts a wavy shape because of the constraint provided by the thin exterior layers, which are stiffer and swell less. Remarkably, we find that if the layered plate is designed to trigger the first buckling mode (i.e., a half sinusoid), it significantly shortens when swollen beyond the instability point. We then demonstrate both numerically and experimentally that such a heterogeneous layered plate can be used as building block to form architected materials with effective negative swelling ratios (see Figure 1b), providing a new mechanism to control the volume of soft structures.

To illustrate the concept, we focused on plates fabricated from two elastomers with significantly different stiffness and swelling characteristics. In particular, for the middle layer we considered a urethane-based rubber (Vytaflex 10 from Smooth-On, Inc) with initial Young modulus E_b = 0.15 MPa, while for the two thin external layers we chose a urethane adhesive (Urebond II from Smooth-On, Inc) with E_a = 10.8 MPa, so that E_a/E_b = 72 (see Supporting Information for details). We also characterized the swellability of the two materials by immersing blocks made of the individual elastomers into an organic solvent (toluene) and monitoring the evolution of their length. Both materials were found to expand, but the strains induced by swelling, $\varepsilon_{sw} = (l - L)/L$ (l and L denoting the length of the sample in the swollen and dry state, respectively) were significantly different, with $\epsilon^{a}_{sw}/\epsilon^{b}_{sw} = 0.116$ (see Supporting Information for details).

We began by investigating the deformation mechanism of an individual layered plate. Assuming that each layer may be described as a thin plate of length L, height h_γ ($\gamma = a, b$), and thickness t made of an elastic material with Young's modulus E_γ, Poisson's ratio ν_γ, and bending stiffness $D_\gamma = E_\gamma t^3/[12(1-\nu_\gamma^2)]$, its buckling behavior can be described by

$$\frac{\partial^4 w_\gamma}{\partial x^4} + 2\frac{\partial^4 w_\gamma}{\partial x^2 \partial y^2} + \frac{\partial^4 w_\gamma}{\partial y^4} = \frac{E_\gamma t g_\gamma}{D_\gamma}\frac{\partial^2 w_\gamma}{\partial x^2}, \quad \text{with } \gamma = a, b \tag{1}$$

where w_γ denotes the out-of-plane deflection of the γ-th layer and g_γ is a function that characterizes the difference in swelling strain between adjacent layers (see Supporting Information). When we consider the plate to be simply supported at the two vertical edges (i.e., $w_\gamma = 0$ and $(\partial^2 w_\gamma/\partial x^2) + \nu_\gamma(\partial^2 w_\gamma/\partial y^2) = 0$ at $x = 0$

Dr. J. Liu, T. Gu, Dr. S. Shan, Prof. K. Bertoldi
Harvard John A. Paulson School of Engineering and Applied Sciences
Harvard University
Cambridge, MA 02138, USA
E-mail: bertoldi@seas.harvard.edu
Prof. S. H. Kang
Department of Mechanical Engineering
Johns Hopkins University
Baltimore, MD 21218, USA
Dr. J. C. Weaver
Wyss Institute for Biologically Inspired Engineering
Harvard University
Cambridge, MA 02138, USA
Prof. K. Bertoldi
Kavli Institute
Harvard University
Cambridge, MA 02138, USA

DOI: 10.1002/adma.201600812

ADVANCED MATERIALS
www.advmat.de

Materials Views
www.MaterialsViews.com

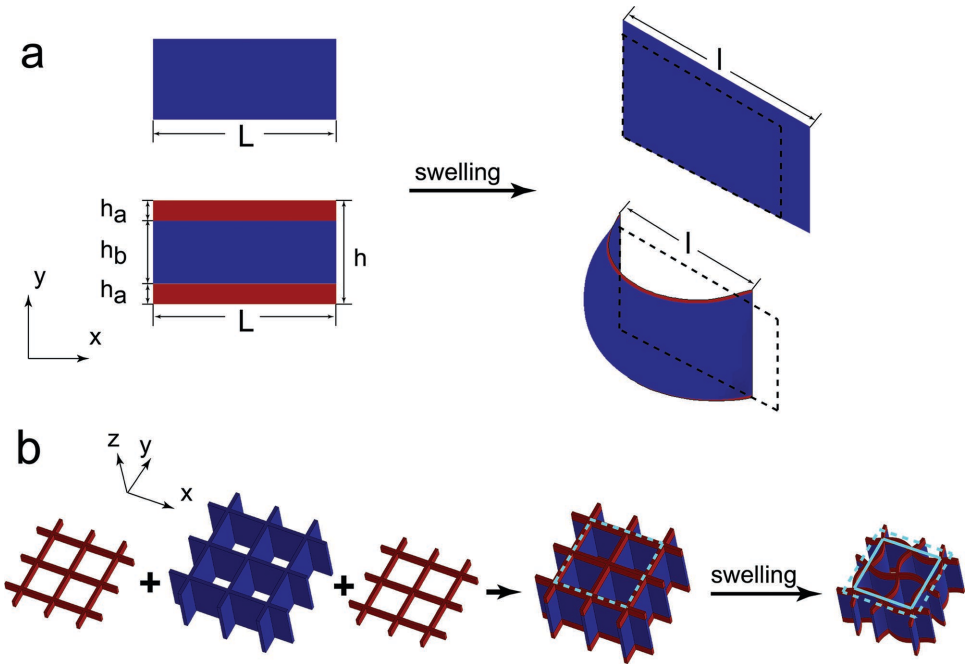

Figure 1. Mechanism to achieve negative swelling. a) A thin plate made of a single material simply expands and preserves its shape when immersed into a solvent. Differently, a layered plate made of two materials with different mechanical properties may buckle and bend out of plane. As a result, its the end-to-end distance that may decrease. The dashed rectangles indicate the initial size of the plate. b) An architected material formed by such layered plates shrinks when imbibing solvent.

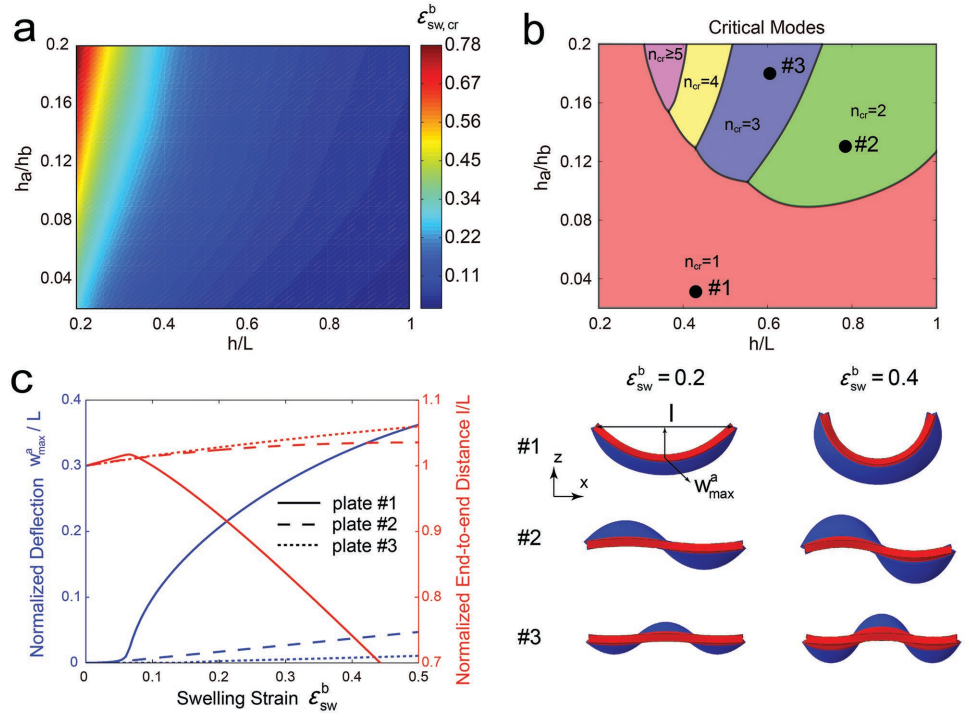

Figure 2. Buckling and postbuckling behavior of a single layered plate. a) Critical swelling strain, $\varepsilon^b_{sw,cr}$, for a layered plate with $t/L = 0.05$ as a function of h/L and h_a/h_b. b) Critical mode, n_{cr}, for a layered plate with $t/L = 0.05$ as a function of h/L and h_a/h_b. Regions characterized by different critical modes are identified using different colors. Note that n_{cr} denotes the number of half-sinusoids in the buckled configuration. c) Evolution of the normalized maximum deflection of the stiff outer layers, w^a_{max}/L (blue, left) and normalized end-to-end distance, l/L (red, right) during the swelling process. Three different configurations are considered: plate #1 (solid lines), plate #2 (dashed lines), and plate #3 (dotted lines). Snapshots at $\epsilon^b_{sw} = 0.2$ and $\epsilon^b_{sw} = 0.4$ are shown on the right.

DOI: 10.1002/adma.201600812

and $x = L$), the solution of Equation (1) has the form $w_\gamma = f_\gamma(y) \sin(n\pi x/L)$, n being an integer (see Supporting Information for details). Imposing continuity conditions at the interfaces between the three layers, the critical swelling strain, $\epsilon^{a}_{\mathrm{sw,cr}}$, and the corresponding mode number, n_{cr}, can then be solved as a function of the aspect ratio h/L ($h = h_a + 2h_b$) and height ratio h_a/h_b, as shown in **Figure 2**a,b for a plate characterized by $t/L = 0.05$, $E_a/E_b = 72$, and $\epsilon^{a}_{\mathrm{sw}}/\epsilon^{b}_{\mathrm{sw}} = 0.116$. The plots reveal that both h/L and h_a/h_b significantly affect not only the the critical swelling strain (see Figure 2a), but also the critical mode (see Figure 2b). A buckling pattern with half sinusoidal wavelength (i.e., $n = 1$) is found for plates that are either very elongated (i.e., for small values of h/L) or characterized by thin external layers (i.e., for small values of h_a/h_b). In addition, higher order modes comprising multiple half-sinusoids are expected to emerge for relatively large values of h/L and h_a/h_b.

Next, we investigated the large deformation behavior of individual layered plates through numerical simulations conducted within the nonlinear finite element (FE) code ABAQUS/Standard, focusing on how buckling affects the evolution of their end-to-end distance. In all our numerical analysis the mechanical response of the elastomers used to fabricate the structure was modeled using a nearly incompressible Neo-Hookean model[33] with initial shear modulus $\mu_\gamma = E_\gamma/3$ ($\gamma = a, b$) and extremely high bulk modulus $K_\gamma = 1000\mu_\gamma$, while their swelling was captured using a thermal analogy (i.e., assuming $\varepsilon_{\mathrm{sw}} = \alpha\Delta T$, where α and ΔT denote the thermal expansion coefficient and temperature increase, respectively). 3D models of the layered plates were constructed using 20-node quadratic brick continuum elements (ABAQUS element type C3D20R) and an imperfection in the form of the critical eigenmode was introduced into the mesh to capture their postbuckling behavior (see Supporting Information for details).

In Figure 2c, we report the evolution of both the normalized end-to-end distance, l/L, and the normalized maximum deflection of the stiff outer layers, $w^{a}_{\max}/L$, for three three different individual plates (highlighted by markers in Figure 2b): plate #1 characterized by (h_a/h_b, h/L) = (0.033, 0.43), plate #2 characterized by (h_a/h_b, h/L) = (0.13, 0.78), and plate #3 characterized by (h_a/h_b, h/L) = (0.18, 0.59). Initially, all three plates are found to expand and increase their length (see Figure 2c). However, when swollen beyond their critical strain, the response of the three plates is distinctly different. For plate #1, which buckles into the first mode, the amplitude of the sinusoidal pattern is found to significantly increase as swelling proceeds, inducing significant bending (see Figure 2c,d). Importantly, such deformation results in a decrease of the end-to-end distance l, which becomes even smaller than that of the undeformed configuration (i.e., $l/L = 0.75$ at $\epsilon^{b}_{\mathrm{sw}} = 0.4$). By contrast, when higher modes are triggered during swelling, as for plates #2 and #3, the amplitude of the buckling mode is observed to slightly increase and does not significantly impact l, which keeps increasing although at a slower pace.

Having demonstrated that a layered plate designed to buckle into the first mode shortens as it imbibes more solvent, we now show that this fact can be exploited to design 2D architected materials with effective negative swelling ratio. We started by investigating both numerically and experimentally the response of a square array of plates. On the numerical side, we conducted nonlinear FE simulations on representative volume elements (see **Figure 3**b,c) with suitable periodic boundary conditions[34,35] (see Supporting Information for details) and calculate the effective swelling strain for the lattice $\overline{\varepsilon}_{\mathrm{sw}}$ directly from the the macroscopic strains $\overline{\varepsilon}_{xx}$ and $\overline{\varepsilon}_{yy}$ as

$$\overline{\varepsilon}_{\mathrm{sw}} = \sqrt{(1+\overline{\varepsilon}_{xx})(1+\overline{\varepsilon}_{yy})} - 1. \tag{2}$$

Furthermore, we experimentally tested the response of square lattices characterized by $L = 30$ mm, which were fabricated using a molding approach (see Supporting Information for details). In all our experiments, the samples were immersed in toluene and the position of the vertices in their central part (highlighted by the red dashed square in Figure 3b,c) was recorded using a high-resolution digital camera and then analyzed by digital image processing (Matlab). Local values of the deformed area $A^{[i,j]}$ for the [ith, jth] square within the area of interest were calculated from the positions of the vertices, $(x^{(i,j)}, y^{(i,j)})$ (see Figure 3b), as

$$A^{[i,j]} = \frac{1}{2}\left|\mathbf{a}_1^{[i,j]} \times \mathbf{a}_2^{[i,j]}\right| + \frac{1}{2}\left|\mathbf{b}_1^{[i,j]} \times \mathbf{b}_2^{[i,j]}\right|, \tag{3}$$

where $i, j = 1, 2$, and

$$\begin{aligned}
\mathbf{a}_1^{[i,j]} &= (x^{(i,j+1)} - x^{(i,j)})\mathbf{e}_x + (y^{(i,j+1)} - y^{(i,j)})\mathbf{e}_y,\\
\mathbf{a}_2^{[i,j]} &= (x^{(i+1,j)} - x^{(i,j)})\mathbf{e}_x + (y^{(i+1,j)} - y^{(i,j)})\mathbf{e}_y,\\
\mathbf{b}_1^{[i,j]} &= (x^{(i,j+1)} - x^{(i+1,j+1)})\mathbf{e}_x + (y^{(i,j+1)} - y^{(i+1,j+1)})\mathbf{e}_y,\\
\mathbf{b}_2^{[i,j]} &= (x^{(i+1,j)} - x^{(i+1,j+1)})\mathbf{e}_x + (y^{(i+1,j)} - y^{(i+1,j+1)})\mathbf{e}_y.
\end{aligned} \tag{4}$$

The swelling strain for the [i-th, j-th] square was then obtained as

$$\varepsilon_{\mathrm{sw}}^{[i,j]} = \sqrt{\frac{A^{[i,j]}}{L^2}} - 1, \tag{5}$$

from which the ensemble average for the central area under consideration was computed, $\overline{\varepsilon}_{\mathrm{sw}} = \langle \varepsilon_{\mathrm{sw}}^{[i,j]} \rangle$.

In Figure 3b,c we report numerical and experimental snapshots taken during the swelling process for lattices formed by plates #1 and #3, while in Figure 3d,e we show the evolution of their macroscopic swelling strain, $\overline{\epsilon}_{\mathrm{sw}}$. Importantly, the snapshots reveal that in both architected materials each plate deforms as when swollen individually. As a result, the area of the lattice made of plate #1 first increase (i.e., $\overline{\epsilon}_{\mathrm{sw}} > 0$) and then, once buckling is triggered, decreases and becomes smaller than that of the original configuration (i.e., $\overline{\epsilon}_{\mathrm{sw}} < 0$). Differently, the lattice made of plate #3 monotonically expands during the swelling process, as the amplitude of the buckled pattern remains small and the individual plates do not shorten. Finally, we note the excellent qualitative and quantitative agreement between experimental and FE results, indicating that numerical simulations can be efficiently used to design architected materials with effective negative swelling ratio.

While in Figure 3 we focused on a square lattice, the proposed mechanism to achieve effective negative swelling is

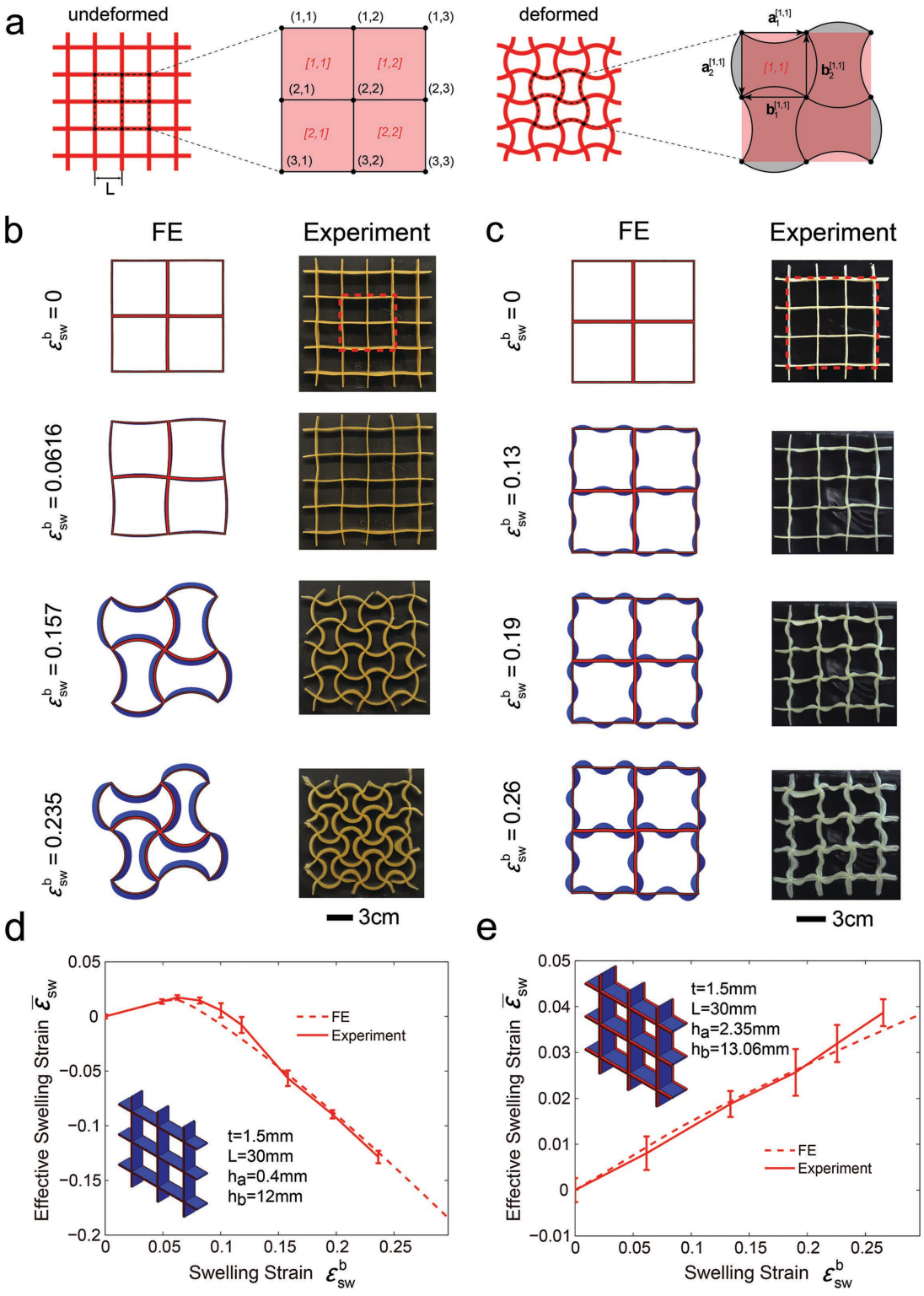

Figure 3. Square lattice. a) Schematic diagrams highlighting the central region with four squares that is used to calculate $\bar{\varepsilon}_{cr}$. The vectors $\mathbf{a}_1^{[i,j]}$, $\mathbf{a}_2^{[i,j]}$, $\mathbf{b}_1^{[i,j]}$ and $\mathbf{b}_2^{[i,j]}$ are indicated on the schematic of the deformed configuration. b) Numerical (left) and experimental (right) snapshots during the swelling process for a square lattice made of plate #1. The dashed red square indicates the cells that are used to calculate $\bar{\varepsilon}_{sw}$. c) Numerical (left) and experimental (right) snapshots during the swelling process for a square lattice made of plate #3. The dashed red square indicates the cells that are used to calculate $\bar{\varepsilon}_{sw}$. d) Evolution of $\bar{\varepsilon}_{sw}$ during the swelling process for a square lattice made of plate #1. Both numerical (dashed line) and experimental (continuous line) are reported. e) Evolution of $\bar{\varepsilon}_{sw}$ during the swelling process for a square lattice made of plate #3. Both numerical (dashed line) and experimental (continuous line) are reported.

Adv. Mater. **2016**,
DOI: 10.1002/adma.201600812

plate-based and thus not restricted to this specific geometry. In fact, any architected material in which all plates can simultaneously buckle into a half sinusoid is expected to exhibit identical behavior and shrink when immersed into a solvent. Such buckled pattern can be supported by unfrustrated lattices with cells formed by an even number of plates (such as the square and the hexagonal lattices). Differently, since in geometrically frustrated lattices comprising cells with an odd number of edges (such as the triangular lattice) not all plates can buckle into a half sinusoid,[36] we expect such configurations not to shrink as much during swelling. To demonstrate this, in **Figure 4** we report numerical results for an unfrustrated hexagonal lattice and a frustrated triangular lattice, both made out of plate #1. The snapshots shown in Figure 4a for the hexagonal geometry indicate that each plate buckle into the first mode (a half sinusoid), resulting in the formation of a three-sided stars pattern. Differently, in the triangular configuration some of the plates buckle into the first mode and some into the second one, forming a chiral pattern similar to that observed previously in equibiaxially compressed beam lattices[36] (Figure 4b). Importantly, we also find that the evolution of $\overline{\varepsilon}_{sw}$ during the swelling process for the hexagonal lattice is exactly the same as that observed for the square lattice, while for the triangular configuration shrinkage is significantly compromised (see Figure 4c), since the plates that buckle into the second mode do not shorten during swelling.

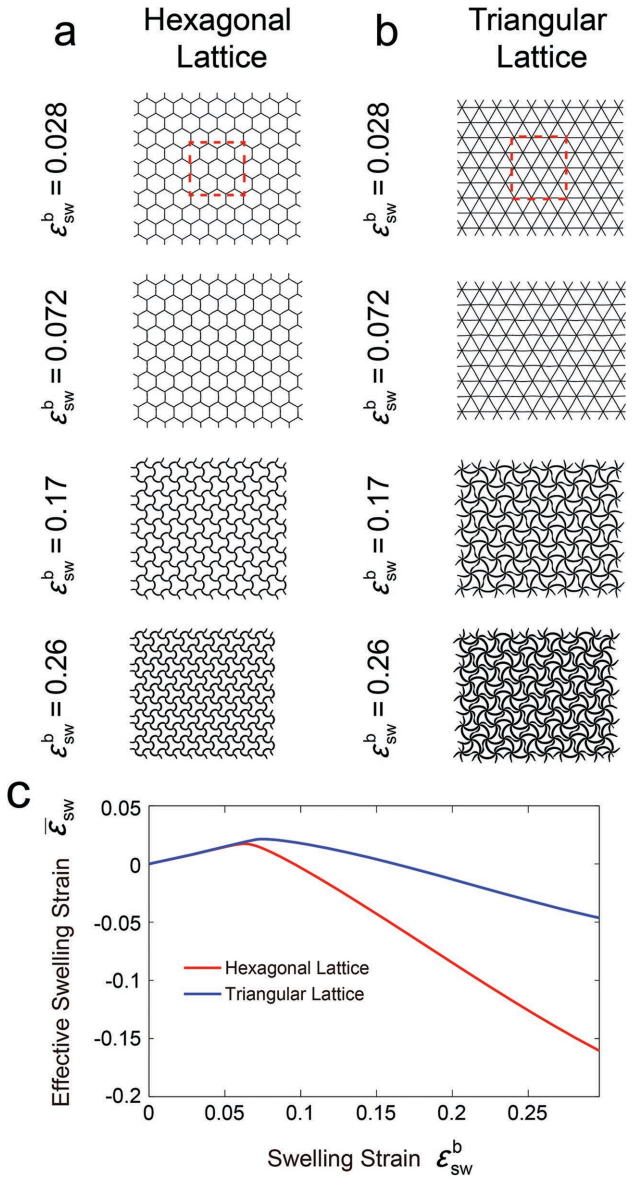

Figure 4. Hexagonal and triangular lattices. a) Numerical snapshots during the swelling process for an hexagonal lattice made of plate #1. The dashed red square indicates the cells that are used to calculate $\overline{\varepsilon}_{sw}$. b) Numerical snapshots during the swelling process for a triangular lattice made of plate #1. c) Evolution of $\overline{\varepsilon}_{sw}$ during the swelling process for an hexagonal (red) and triangular (blue) lattice made of plate #1.

In summary, we have proposed a new mechanism based on buckling to induce effective negative swelling in architected materials. Remarkably, this mechanism is scale free and can be applied to structures with various length scales. While in Figure 3 we have shown results for a square lattice at the centimeter length-scale, identical behavior can be also observed at smaller scale, as shown in Figure S9 (Supporting Information) for a square and hexagonal lattice with L = 2 mm fabricated using projection microstereolithography[37] (see Supporting Information for more details). Furthermore, although here we have focused on swelling, the same design principles can be extended to different materials and stimuli (e.g., temperature, pH, and light), so that they can be used to systematically alter the changes in area and volume experienced by a broad class of material systems. For example, although several designs have been reported to achieve negative thermal expansion,[30–32,38–45] our simple design may yield a more efficient fabrication process of materials that shrink when subjected to a temperature increase and also enables tunability of the response. Finally, the proposed mechanism works for a large number of geometries (i.e., for all unfrustrated lattices) and our multilayer design is simple and modular, as the changes in area of the material can be tuned by controlling geometric parameters guided by a "phase diagram." Hence, our findings open new opportunities for the design of materials and structures capable of achieving targeted and extreme area/volume changes, as required for a number of aerospace,[46,47] optical,[48,49] energy,[50,51] and microelectronic[52,53] applications.

Supporting Information

Supporting Information is available from the Wiley Online Library or from the author.

Acknowledgements

This work was supported by Harvard MRSEC through grant DMR-1420570 and NSF through grant CMMI-1149456 (CAREER). The authors are also grateful to Howon Lee and Jianyu Li for inspirational discussions and help.

Received: February 10, 2016
Revised: April 8, 2016
Published online:

[1] B. H. Cipriano , S. J. Banik, R. Sharma, D. Rumore, W. Hwang, R. M. Briber, S. R. Raghavan, *Macromolecules* **2014**, *47*, 4445.
[2] T. K. Mudiyanselage, D. C. Neckers, *Soft Matter* **2008**, *4*, 768.
[3] T. Ono, T. Sugimoto, S. Shinkai, K. Sada, *Nat. Mater.* **2007**, *6*, 429.
[4] J. N. Lee, C. Park, G. M. Whitesides, *Anal. Chem.* **2003**, *75*, 6544.
[5] A. Sidorenko, T. Krupenkin, A. Taylor, P. Fratzl, J. Aizenberg, *Science* **2007**, *315*, 487.
[6] A. Sidorenko, T. Krupenkin, J. Aizenberg, *J. Mater. Chem.* **2008**, *18*, 3841.
[7] S. Maeda, Y. Hara, T. Sakai, R. Yoshida, S. Hashimoto, *Adv. Mater.* **2007**, *19*, 3480.
[8] S. Maeda, Y. Hara, R. Yoshida, S. Hashimoto, *Macromol. Rapid Commun.* **2008**, *29*, 401.
[9] J. HeeáLee, Z. Stephen et al., *J. Mater. Chem.* **2011**, *21*, 6824.
[10] S. Turcaud, L. Guiducci, P. Fratzl, Y. J. Bréchet, J. W. Dunlop, *Int. J. Mater. Res.* **2011**, *102*, 607.
[11] H. Lee, C. Xia, N. X. Fang, *Soft Matter* **2010**, *6*, 4342.
[12] R. F. Freitas, E. Cussler, *Chem. Eng. Sci.* **1987**, *42*, 97.
[13] E. Cussler, M. Stokar, J. Varberg, *AIChE J.* **1984**, *30*, 578.
[14] T. G. Park, A. S. Hoffman, *Macromolecules* **1993**, *26*, 5045.
[15] K. Sawahata, M. Hara, H. Yasunaga, Y. Osada, *J. Control. Rel.* **1990**, *14*, 253.
[16] D. J. Beebe et al., *Nature* **2000**, *404*, 588.
[17] K.-F. Arndt, D. Kuckling, A. Richter, *Polym. Adv. Technol.* **2000**, *11*, 496.
[18] A. Richter, S. Klatt, G. Paschew, C. Klenke, *Lab Chip* **2009**, *9*, 613.
[19] R. Bashir, J. Hilt, O. Elibol, A. Gupta, N. Peppas, *Appl. Phys. Lett.* **2002**, *81*, 3091.
[20] F. Zee, J. W. Judy, *Sens. Actuat. B: Chem.* **2001**, *72*, 120.
[21] K. Deligkaris, T. S. Tadele, W. Olthuis, A. van den Berg, *Sens. Actuat. B: Chem.* **2010**, *147*, 765.
[22] A. Richter et al., *Sensors* **2008**, *8*, 561.
[23] J. Kopeček, J. Yang, *Polym. Int.* **2007**, *56*, 1078.
[24] N. A. Peppas, J. Z. Hilt, A. Khademhosseini, R. Langer, *Adv. Mater.* **2006**, *18*, 1345.
[25] R. Kishi, H. Ichijo, O. Hirasa, *J. Intell. Mater. Syst. Struct.* **1993**, *4*, 533.
[26] K. Kajiwara, S. B. Ross-Murphy, *Nature* **1992**, *355*, 208.
[27] Y. Osada, H. Okuzaki, H. Hori, *Nature* **1992**, *355*, 242.
[28] N. Terasawa, I. Takeuchi, H. Matsumoto, *Sens. Actuat. B: Chem.* **2009**, *139*, 624.
[29] D. G. Barrett, G. G. Bushnell, P. B. Messersmith, *Adv. Healthcare Mater.* **2013**, *2*, 745.
[30] R. Lakes, *J. Mater. Sci. Lett.* **1996**, *15*, 475.
[31] R. Lakes, *Appl. Phys. Lett.* **2007**, *90*, 221905.
[32] G. Jefferson, T. A. Parthasarathy, R. J. Kerans, *Int. J. Solids Struct.* **2009**, *46*, 2372.
[33] R. S. Rivlin, D. Saunders, *Philos. Trans. R. Soc. London A: Math., Phys. Eng. Sci.* **1951**, *243*, 251.
[34] M. Danielsson, D. Parks, M. Boyce, *J. Mech. Phys. Solids* **2002**, *50*, 351.
[35] K. Bertoldi, M. Boyce, S. Deschanel, S. Prange, T. Mullin, *J. Mech. Phys. Solids* **2008**, *56*, 2642.
[36] S. H. Kang et al., *Phys. Rev. Lett.* **2014**, *112*, 098701.
[37] C. Sun, N. Fang, D. Wu, X. Zhang, *Sens. Actuat. A: Phys.* **2005**, *121*, 113.
[38] C. A. Steeves et al., *J. Mech. Phys. Solids* **2007**, *55*, 1803.
[39] T.-C. Lim, *J. Mater. Sci.* **2012**, *47*, 368.
[40] T.-C. Lim, *J. Mater. Sci.* **2005**, *40*, 3275.
[41] T.-C. Lim, *Phys. Stat. Solidi (B)* **2013**, *250*, 2062.
[42] J. N. Grima, P. S. Farrugia, R. Gatt, V. Zammit, *Proc. R. Soc. London A: Math., Phys. Eng. Sci.* **2007**, *463*, 1585.
[43] J. Berger, C. Mercer, R. M. McMeeking, A. G. Evans, *J. Am. Ceramic Soc.* **2011**, *94*, S42.
[44] O. Sigmund, S. Torquato, *Appl. Phys. Lett.* **1996**, *69*, 3203.
[45] J. Qi, J. Halloran, *J. Mater. Sci.* **2004**, *39*, 4113.
[46] G. Jefferson, T. A. Parthasarathy, R. J. Kerans, *Int. J. Solids Struct.* **2009**, *46*, 2372.
[47] P. M. Jacquot, M. Lehmann, X. C. de Lega, *International Society for Optics and Photonics*, **1998**, pp. 102–113.
[48] R. Bastaits, G. Rodrigues, P. Jetteur, P. Hagedorn, A. Preumont, *Smart Mater. Struct.* **2012**, *21*, 064004.
[49] K. Patterson, S. Pellegrino, *Appl. Opt.* **2013**, *52*, 5327.
[50] K. Zweibel, *Solar Energy Mater. Solar Cells* **2000**, *63*, 375.
[51] K. Chopra, P. Paulson, V. Dutta et al., *Progr. Photovolt.* **2004**, *12*, 69.
[52] C. Zweben, *Jom* **1998**, *50*, 47.
[53] M. R. Werner, W. R. Fahrner, *IEEE Trans. Industr. Electron.* **2001**, *48*, 249.

Adv. Mater. **2016**,
DOI: 10.1002/adma.201600812

ADVANCED MATERIALS

Supporting Information

for *Adv. Mater.*, DOI: 10.1002/adma.201600812

Harnessing Buckling to Design Architected Materials that Exhibit Effective Negative Swelling

*Jia Liu, Tianyu Gu, Sicong Shan, Sung H. Kang, James C. Weaver, and Katia Bertoldi**

Supplementary Materials for
Harnessing buckling to design architected materials that exhibit effective negative swelling

Jia Liu,[1] Tianyu Gu,[1] Sicong Shan,[1] Sung H. Kang,[2] James C. Weaver,[3] and Katia Bertoldi[1,4]

[1]*Harvard John A. Paulson School of Engineering and Applied Sciences, Harvard University, Cambridge, MA 02138*
[2]*Department of Mechanical Engineering, Johns Hopkins University, Baltimore, MD 21218*
[3]*Wyss Institute for Biologically Inspired Engineering, Harvard University, Cambridge, Massachusetts 02138*
[4]*Kavli Institute, Harvard University, Cambridge, Massachusetts 02138, USA*

(Dated: February 10, 2016)

FABRICATION

We first describe the molding approach used to fabricate most of our structures, followed by a brief description of the manufacture of smaller structures using projection micro-stereolithography.

Molding approach

To manufacture centimeter-scale structures exhibiting negative negative swelling a molding approach is used. First, a negative mold was fabricated using a 3D printer (Connex 500 available from Objet, Ltd.) with VeroBlue (product number: RGD840, Objet) material. Then, the structures were cast using silicone rubbers (Urebond II from Smooth-On for the outer, stiff layers and Vytaflex 10 from Smooth-On for the central, soft layers). Before replication, a releasing agent (Easy Release 200 available from Smooth-On, Inc.) was sprayed on to the molds for easy separation. To fabricate the three layered structure, the outer layers were first casted using a shorter mold and cured. Afterwards, one of the cured outer layers was inserted into the bottom of a larger mold and the central layer was casted, and then covered by the other cured outer layer. The full sample was again cured before it was taken out. In the resulting structure, each plate has length $L = 30$ mm and thickness $t = 1.5$ mm.

Mechanical properties of Urebond II and Vytaflex 10. Dogbone samples made of Urebond II and Vytaflex 10 were tested in the dry state under uniaxial tension using a single-axis Instron. The tests show that the materials exhibits a behavior typical for elastomers: large strain elastic behavior with negligible rate dependence and negligible hysteresis during a loading-unloading cycle. The material behavior at a strain rate of 0.0003 s^{-1} is reported in Fig. S1 (note that to quantify the applied stretch, dark markers were placed on the samples whose position was digitally tracked during the tests). The observed constitutive behavior is modeled as hyperelastic. In particular, their stress-strain response is captured using an incompressible Neo-Hookean model, whose strain energy is given by

$$W = \frac{\mu}{2}(I_1 - 3), \tag{S1}$$

where μ is the initial shear modulus. Moreover, $I_1 = \mathrm{tr}\,\mathbf{F}^T\mathbf{F}$, where $\mathbf{F} = \partial\mathbf{x}/\partial\mathbf{X}$ denotes the deformation gradient —a linear transformation which maps a material point from its reference position $\mathbf{X}$ to its current location $\mathbf{x}$. Under uniaxial tension the axial nominal stress, s_{11}, is given by

$$s_{11} = \mu\left(\lambda - \frac{1}{\lambda^2}\right), \tag{S2}$$

where λ is applied stretch, defined as the deformed length over the initial length.

From the uniaxial tension data shown in Fig. S1, the initial shear modulus was measured to be $\mu = 3.6$ MPa for Urebond II and $\mu = 0.05$ MPa for Vytaflex 10. Fig. S1 shows that the Neo-Hookean model captures the behavior very well up to a strain of about 1.4 for Vytaflex 10 and 1.05 for Urebond II, which cover the majority of the strain levels studied. Finally, we note that for an incompressible materials the Poisson's ratio is one half ($\nu = 0.5$), so that the Young's moduli of Urebond II and Vytaflex 10 are given by $E_a = 2(1 + \nu_a)\mu_a = 10.8$ MPa and $E_b = 2(1 + \nu_b)\mu_b = 0.15$ MPa, respectively.

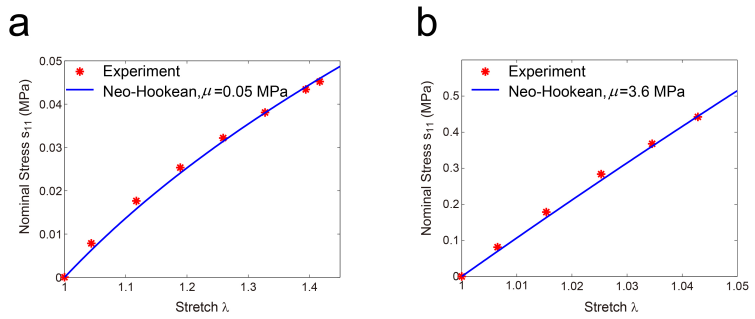

FIG. S1: Stress-strain curves for (a) Vytaflex 10 and (b) Urebond II as measured experimentally (red markers) and predicted by the Neo-Hookean model (blue lines).

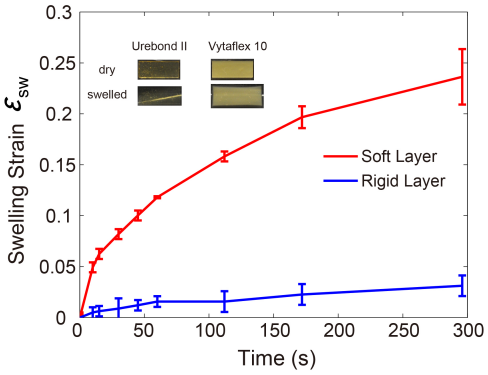

FIG. S2: Experimentally measured swelling strain as a function of time for both Vytaflex 10 (red line) and Urebond II (blue line).

Swellability of Urebond II and Vytaflex 10. To quantify the swellability of Urebond II and Vytaflex 10, rectangular control samples of W(width) × H(height) × D(thickness) = 30 × 12 × 1.5 mm were fabricated out of the two materials. The samples (one rigid and one soft) were then immersed into the organic solvent toluene and their swelling recorded using a high resolution digital SLR camera (Nikon D90) positioned above them. The swelling strains of the samples was measured by tracking their lengths.

Fig. S2 shows the swelling strain curves obtained for the two materials. The data clearly indicate that Vytaflex 10 swells significantly more than Urebond II.

Projection micro-stereolithography

We used projection micro-stereolithography (PμSL) to fabricate millimiter-scale samples. PμSL is a digital freeform microfabrication technology capable of fabricating complex shaped 3D micro architectures by using a dynamic mask generator and an UV light source coupled to a projection lens system to convert liquid monomer to solid polymer in an additive, layer-by-layer fashion. Fig. S3 shows a schematic of the custom-built PμSL apparatus. Note that the typical size of the structures fabricated for this study is 14.4 mm(W) × 14.4 mm(L) × 1.4 mm(H) with a layer thickness of 120 μm.

The prepolymer solution used to make the structures consists of 33.5 wt. % poly (ethylene glycol) diacrylate (PEGDA 585, from Sigma-Aldrich), 65.78 wt. % poly (ethylene glycol) (PEG 200, from Sigma-Aldrich), 0.67 wt. % photoinitiator (BAPO, from Sigma-Aldrich) and 0.05 wt. % photoabsorber (Sudan-I, from Sigma-Aldrich). Note that PEG is added to increase the swelling ratio of the material, since it does not polymerize during photo-polymerization and occupies intermolecular space between PEGDA, lowering the cross linking density. After fabrication is completed, PEG is then removed from the structure by immersing the samples into acetone for 2 hours. Following this procedure a swelling ratio of approximately $\varepsilon_{sw} = l/L \simeq 1.5$ is obtained (differently, if PEG is not removed from the samples $\varepsilon_{sw} = l/L \simeq 1.1$).

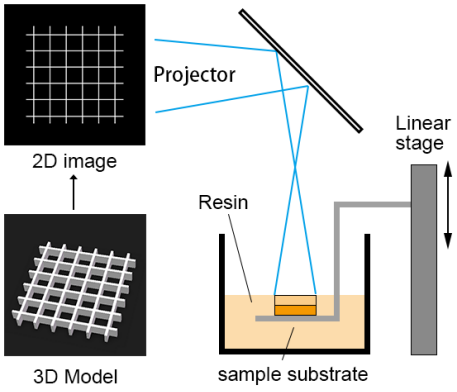

FIG. S3: Schematic of the PμSL apparatus

Finally, the top and bottom surfaces of the samples are treated with UV light [133mW/cm^2] for 30 minutes to increase their polymerization and reduce their swelling ratio to $\varepsilon_{sw} = l/L \simeq 1.1$. Following this process the Young's modulus of the outer layers is increased to $E = 12.5$ MPa, while for the central (not UV cured) part of the samples $E = 2.5$ MPa. Note that the penetration depth of UV light is controlled by covering the sample with the photoabsorber and tuning its concentration. Here, the penetration depth of UV light is chosen so that all plates buckle into the first more (a half sinusoidal).

BUCKLING-INDUCED NEGATIVE SWELLING IN MILLI-SCALE SAMPLES

The response of the samples fabricated using PμSL under swelling was tested by placing them on a dry glass slide and dropping solvent (acetone) on them. The swelling was recorded by a digital SLR camera (Nikon D90) placed underneath the glass slide. Each frame of the recorded video was then extracted and processed in Matlab as described in the main text.

In Fig. S4 we show two snapshots of a square and hexagonal lattices designed to achieve effective negative swelling (for these samples $h_a = 0.2$ mm, $h_b = 0.8$ mm, $L = 2$ mm, $t = 0.1$ mm), showing a deformation very similar to that reported in the main text for larger scale structures.

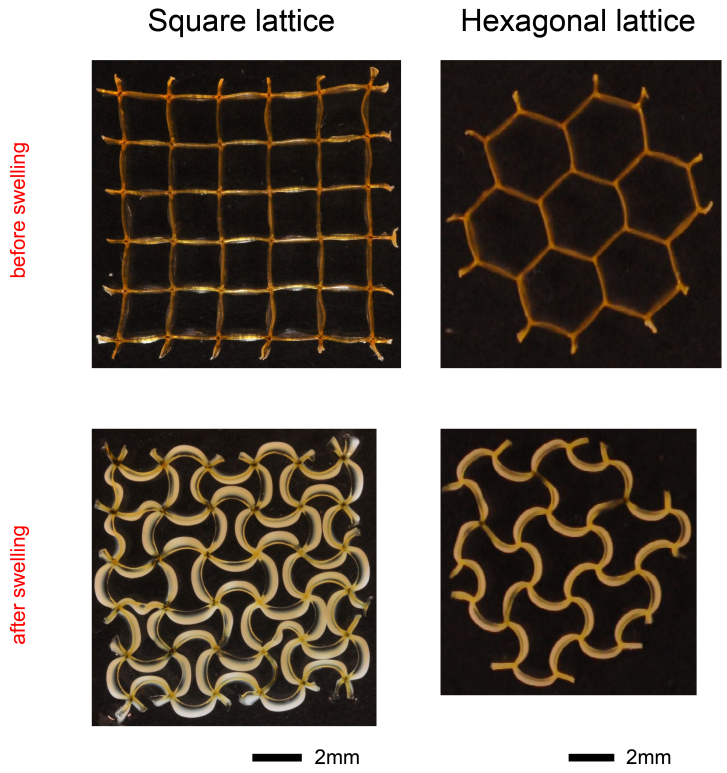

FIG. S4: Experimental snapshots during the swelling process for a square (left) and an hexagonal lattice fabricated using PμSL.

BUCKLING OF A SINGLE LAYERED PLATE: ANALYTICAL SOLUTION

In this Section we investigate analytically the buckling behavior of an individual layered plate subjected to isotropic swelling. The plate has length L and comprises two outer layers of height h_a and a central layer of height h_b (see Fig. S5). Moreover, the plate is considered to be thin, namely $t \ll L, h_a, h_b$. Finally, we assume that each layer is made of an elastic material with Young's modulus E_γ, Poisson's ratio ν_γ and bending stiffness $D_\gamma = E_\gamma t^3/[12(1-\nu_\gamma^2)]$, with $\gamma = a, b$.

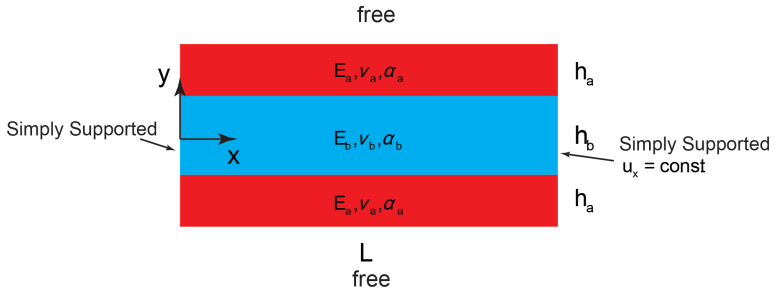

FIG. S5: Schematic of the layered plate.

Plate equation. Under such assumptions, the buckling behavior of each layer can be investigated by solving the plate equation [1] (note that in the following, for the sake of simplicity, the subscript γ has been omitted)

$$\frac{\partial^4 w}{\partial x^4} + 2\frac{\partial^4 w}{\partial x^2 \partial y^2} + \frac{\partial^4 w}{\partial y^4} = \frac{1}{D}\left(p + N_{xx}\frac{\partial^2 w}{\partial x^2} + N_{yy}\frac{\partial^2 w}{\partial y^2} + 2N_{xy}\frac{\partial^2 w}{\partial x \partial y}\right), \tag{S3}$$

where w denotes the out-of-plane deflection of the layer and p is the applied pressure, which in this case is zero. Moreover, N_{xx}, N_{yy} and N_{xy} are the in-plane stress resultants, which are given by

$$N_{xx} = \int_{-t/2}^{t/2} \sigma_{xx}\, dz, \qquad N_{yy} = \int_{-t/2}^{t/2} \sigma_{yy}\, dz, \qquad N_{xy} = \int_{-t/2}^{t/2} \sigma_{xy}\, dz. \tag{S4}$$

The stress components σ_{xx}, σ_{xy} and σ_{yy} are determined assuming the material to be linear elastic and capturing its swelling using a thermal analogy (i.e. assuming $\epsilon_{sw} = \alpha\Delta T$, where α and ΔT denote the thermal expansion coefficient and temperature increase, respectively), so that

$$\begin{aligned}
\sigma_{xx} &= \frac{E}{(1+\nu)(1-2\nu)}\left[\epsilon_{xx}(1-\nu) + \nu(\epsilon_{yy}+\epsilon_{zz})\right] - \frac{E\alpha\Delta T}{1-2\nu}, \\
\sigma_{yy} &= \frac{E}{(1+\nu)(1-2\nu)}\left[\epsilon_{yy}(1-\nu) + \nu(\epsilon_{xx}+\epsilon_{zz})\right] - \frac{E\alpha\Delta T}{1-2\nu}, \\
\sigma_{zz} &= \frac{E}{(1+\nu)(1-2\nu)}\left[\epsilon_{zz}(1-\nu) + \nu(\epsilon_{xx}+\epsilon_{yy})\right] - \frac{E\alpha\Delta T}{1-2\nu}.
\end{aligned} \tag{S5}$$

Moreover, since the shear stress is zero during swelling,

$$\sigma_{xy} = 0. \tag{S6}$$

Finally, since for a thin plate $\sigma_{zz} = 0$, Eq. $(S5)_3$ reduces to

$$\frac{E}{(1+\nu)(1-2\nu)}\epsilon_{zz} = \frac{E\alpha\Delta T}{(1-2\nu)(1-\nu)} - \frac{E\nu(\epsilon_{xx}+\epsilon_{yy})}{(1+\nu)(1-\nu)(1-2\nu)}, \tag{S7}$$

which is substituted into Eqs. $(S5)_{1,2}$ to yield

$$\begin{aligned}
\sigma_{xx} &= \frac{E\epsilon_{xx}}{1-\nu^2} + \frac{\nu E\epsilon_{yy}}{1-\nu^2} - \frac{E\alpha\Delta T}{1-\nu}, \\
\sigma_{yy} &= \frac{E\epsilon_{yy}}{1-\nu^2} + \frac{\nu E\epsilon_{xx}}{1-\nu^2} - \frac{E\alpha\Delta T}{1-\nu}.
\end{aligned} \tag{S8}$$

Boundary conditions. In a 2D cellular structure subjected to isotropic swelling, the top and bottom edges of each plate are traction free (i.e. the shear force and moment on these two edges are zero), so that at $y = -h_a - h_b/2$ and $y = h_a + h_b/2$

$$\frac{\partial^2 w}{\partial y^2} + \nu \frac{\partial^2 w}{\partial x^2} = 0, \tag{S9}$$

and

$$\frac{\partial^3 w}{\partial y^3} + (2-\nu)\frac{\partial^3 w}{\partial x^2 \partial y} = 0. \tag{S10}$$

Moreover, since the plates are free to rotate at the junctions while expanding, we assume that the left edge is simply supported (i.e. displacements are fixed while rotation is allowed), while the right edge is free to rotate and to uniformly move in x-direction. Since all three layers are free to swell in x-direction, the total in-plan stress resultant N_{xx} is zero

$$\int_{-h_a-h_b/2}^{h_a+h_b/2} N_{xx}\, dy = 0, \tag{S11}$$

yielding

$$\sigma_{xx}^a \cdot 2h_a + \sigma_{xx}^b \cdot h_b = 0. \tag{S12}$$

Moreover, since each layer can also freely expand along the y-direction, we expect σ_{yy} to be zero. It follows from Eq. $(S8)_2$ that

$$\epsilon_{yy} = -\nu \epsilon_{xx} + \alpha \Delta T (1+\nu). \tag{S13}$$

Substitution of Eq. (S13) into Eq. $(S8)_1$ yields

$$\sigma_{xx} = E(\epsilon_{xx} - \alpha \Delta T), \tag{S14}$$

which together with Eq. (S12) leads to

$$\epsilon_{xx} = \frac{2E_a h_a \alpha_a + E_b h_b \alpha_b}{2E_a h_a + E_b h_b} \Delta T. \tag{S15}$$

Substituting Eqs. (S15), (S6) and (S8) into Eq. (S4), the in-plane stress resultants are obtained as

$$\begin{aligned} N_{xx}^a = \sigma_{xx}^a \cdot t &= \frac{E_a E_b t \Delta T}{2E_a h_a + E_b h_b} h_b(\alpha_b - \alpha_a), \\ N_{xx}^b = \sigma_{xx}^b \cdot t &= \frac{E_a E_b t \Delta T}{2E_a h_a + E_b h_b} 2h_a(\alpha_a - \alpha_b), \\ N_{yy}^a = N_{yy}^b &= N_{xy}^a = N_{xy}^b = 0. \end{aligned} \tag{S16}$$

Finally, continuity of tractions and displacements has to be enforced at the interfaces between the three layers, yielding

$$\begin{aligned} w\big|_{y=\frac{h_b}{2}^+} &= w\big|_{y=\frac{h_b}{2}^-}, \\ \left.\frac{\partial w}{\partial y}\right|_{y=\frac{h_b}{2}^+} &= \left.\frac{\partial w}{\partial y}\right|_{y=\frac{h_b}{2}^-}, \\ D\left(\frac{\partial^2 w}{\partial y^2} + \nu \frac{\partial^2 w}{\partial x^2}\right)\Big|_{y=\frac{h_b}{2}^+} &= D\left(\frac{\partial^2 w}{\partial y^2} + \nu \frac{\partial^2 w}{\partial x^2}\right)\Big|_{y=\frac{h_b}{2}^-}, \\ D\left(\frac{\partial^3 w}{\partial y^3} + (2-\nu)\frac{\partial^3 w}{\partial x^2 \partial y}\right)\Big|_{y=\frac{h_b}{2}^+} &= D\left(\frac{\partial^3 w}{\partial y^3} + (2-\nu)\frac{\partial^3 w}{\partial x^2 \partial y}\right)\Big|_{y=\frac{h_b}{2}^-}, \end{aligned} \tag{S17}$$

and

$$\begin{aligned} w\big|_{y=-\frac{h_b}{2}^+} &= w\big|_{y=-\frac{h_b}{2}^-}, \\ \left.\frac{\partial w}{\partial y}\right|_{y=-\frac{h_b}{2}^+} &= \left.\frac{\partial w}{\partial y}\right|_{y=-\frac{h_b}{2}^-}, \\ D\left(\frac{\partial^2 w}{\partial y^2}+\nu\frac{\partial^2 w}{\partial x^2}\right)\Big|_{y=-\frac{h_b}{2}^+} &= D(\frac{\partial^2 w}{\partial y^2}+\nu\frac{\partial^2 w}{\partial x^2})\Big|_{y=-\frac{h_b}{2}^-}, \\ D\left(\frac{\partial^3 w}{\partial y^3}+(2-\nu)\frac{\partial^3 w}{\partial x^2\partial y}\right)\Big|_{y=-\frac{h_b}{2}^+} &= D\left(\frac{\partial^3 w}{\partial y^3}+(2-\nu)\frac{\partial^3 w}{\partial x^2\partial y}\right)\Big|_{y=-\frac{h_b}{2}^-}. \end{aligned} \tag{S18}$$

Buckling. Following the general buckling analysis procedure, we assume the out-of-plane deflection w is of the form $w = f(y)\sin(n\pi x/L)$ (n being an integer) and substitute it into Eq. (S3) to obtain

$$f'''' - \frac{2n^2\pi^2}{L^2}f'' + \frac{n^4\pi^4}{L^4}f = -\frac{1}{D}N_{xx}\frac{n^2\pi^2}{L^2}f. \tag{S19}$$

Eq. (S19) is a homogeneous linear ordinary differential equation with constant coefficients, whose solution has the form

$$f = \sum_{i=1^4} Q_i \exp(z_i y), \tag{S20}$$

where Q_i are constant coefficients and z_i are the roots of its characteristic equation

$$\left(z^2 - \frac{n^2\pi^2}{L^2}\right)^2 = -\frac{n^2\pi^2}{L^2}\cdot\frac{N_{xx}}{D}. \tag{S21}$$

Moreover, substitution of the solution, $w_\gamma = f_\gamma(y)\sin(n\pi x/L)$, into the boundary and continuity conditions [Eqs. (S9),(S10),(S17) and (S18)] yields

$$\begin{aligned} \text{at } y = h_a + \frac{h_b}{2}: \ & f''_{a^+} - \nu_a\frac{n^2\pi^2}{L^2}f_{a^+} = 0, \\ & f'''_{a^+} - (2-\nu_a)\frac{n^2\pi^2}{L^2}f'_{a^+} = 0, \\ \text{at } y = -h_a - \frac{h_b}{2}: \ & f''_{a^-} - \nu_a\frac{n^2\pi^2}{L^2}f_{a^-} = 0, \\ & f'''_{a^-} - (2-\nu_a)\frac{n^2\pi^2}{L^2}f'_{a^-} = 0, \\ \text{at } y = \frac{h_b}{2}: \ & f_{a^+} = f_b, \\ & f'_{a^+} = f'_b, \\ & D_a\left(f''_{a^+} - \nu_a\frac{n^2\pi^2}{L^2}f_{a^+}\right) = D_b\left(f''_b - \nu_b\frac{n^2\pi^2}{L^2}f_b\right), \\ & D_a\left(f'''_{a^+} - (2-\nu_a)\frac{n^2\pi^2}{L^2}f'_{a^+}\right) = D_b\left(f'''_b - (2-\nu_b)\frac{n^2\pi^2}{L^2}f'_b\right), \\ \text{at } y = -\frac{h_b}{2}: \ & f_{a^-} = f_b, \\ & f'_{a^-} = f'_b, \\ & D_a\left(f''_{a^-} - \nu_a\frac{n^2\pi^2}{L^2}f_{a^-}\right) = D_b\left(f''_b - \nu_b\frac{n^2\pi^2}{L^2}f_b\right), \\ & D_a\left(f'''_{a^-} - (2-\nu_a)\frac{n^2\pi^2}{L^2}f'_{a^-}\right) = D_b\left(f'''_b - (2-\nu_b)\frac{n^2\pi^2}{L^2}f'_b\right), \end{aligned} \tag{S22}$$

where f_{a^+}, f_b and f_{a^-} denote the solution for the top, middle and bottom layer, respectively.

Finally, we note that the form of the solution in the three layers will be different, depending on whether the roots of Eq. (S21) are real or complex. In particular,

1. if $\dfrac{n^2\pi^2}{L^2} < -\dfrac{N^b_{xx}}{D_b}$ and $(\alpha_b > \alpha_a, \Delta T > 0)$ or $(\alpha_b < \alpha_a, \Delta T < 0)$, so that $N^a_{xx} > 0$ and $N^b_{xx} < 0$, the roots of Eq. (S21) for the top and bottom layers are

$$z = \pm M\cos(\theta/2) \pm i\, M\sin(\theta/2), \tag{S23}$$

where $M = \sqrt{\frac{n\pi}{L}\sqrt{\frac{n^2\pi^2}{L^2} + \frac{1}{D_a}N^a_{xx}}}$, and $\theta = \arctan\sqrt{\frac{N^a_{xx}L}{D_a n^2\pi^2}}$. It follows that the solution for the top and bottom layers is given by:

$$\begin{aligned} f_{a^+} &= A_1\exp(\gamma_a y)\sin(\beta_a y) + A_2\exp(\gamma_a y)\cos(\beta_a y) + \\ &\quad A_3\exp(-\gamma_a y)\sin(\beta_a y) + A_4\exp(-\gamma_a y)\cos(\beta_a y), \\ f_{a^-} &= C_1\exp(\gamma_a y)\sin(\beta_a y) + C_2\exp(\gamma_a y)\cos(\beta_a y) + \\ &\quad C_3\exp(-\gamma_a y)\sin(\beta_a y) + C_4\exp(-\gamma_a y)\cos(\beta_a y). \end{aligned} \tag{S24}$$

where $\gamma_a = M\cos(\theta/2)$ and $\beta_a = M\sin(\theta/2)$.

Moreover, for the middle layer the roots of Eq. (S21) are

$$z = \pm\sqrt{\frac{n^2\pi^2}{L^2} + \sqrt{\frac{n^2\pi^2}{L^2}\frac{-N^b_{xx}}{D_b}}}, \quad z = \pm\sqrt{-\frac{n^2\pi^2}{L^2} + \sqrt{\frac{n^2\pi^2}{L^2}\frac{-N^b_{xx}}{D_b}}}i. \tag{S25}$$

It follows that the solution for the middle layer takes the form

$$f_b = B_1\exp(\gamma_b y) + B_2\exp(-\gamma_b y) + B_3\sin(\beta_b y) + B_4\cos(\beta_b y), \tag{S26}$$

where $\gamma_b = \sqrt{\frac{n^2\pi^2}{L^2} + \sqrt{\frac{n^2\pi^2}{L^2}\frac{-N^b_{xx}}{D_b}}}$ and $\beta_b = \sqrt{-\frac{n^2\pi^2}{L^2} + \sqrt{\frac{n^2\pi^2}{L^2}\frac{-N^b_{xx}}{D_b}}}$.

2. if $\frac{n^2\pi^2}{L^2} = -\frac{N^b_{xx}}{D_b}$ and $(\alpha_b > \alpha_a, \Delta T > 0)$ or $(\alpha_b < \alpha_a, \Delta T < 0)$, so that $N^a_{xx} > 0, N^b_{xx} < 0$, the solution for the top and bottom layers is still given by Eq. (S24). Differently, the roots of Eq. (S21) for middle layer are

$$z = \frac{\sqrt{2}n\pi}{L}, \qquad z = 0. \tag{S27}$$

It follows that the solution for the middle layer takes the form

$$f_b = B_1\exp(\gamma_b y) + B_2\exp(-\gamma_b y) + B_3 + B_4 y, \tag{S28}$$

where $\gamma_b = \frac{\sqrt{2}n\pi}{L}$.

3. if $\frac{n^2\pi^2}{L^2} > -\frac{N^b_{xx}}{D_b}$ and $(\alpha_b > \alpha_a, \Delta T > 0)$ or $(\alpha_b < \alpha_a, \Delta T < 0)$, so that $N^a_{xx} > 0, N^b_{xx} < 0$, the solution for the top and bottom layers is still given by Eq. (S24). Differently, the roots of Eq. (S21) for middle layer are

$$z = \pm\sqrt{\frac{n^2\pi^2}{L^2} + \sqrt{\frac{n^2\pi^2}{L^2}\frac{-N^b_{xx}}{D_b}}}, \qquad z = \pm\sqrt{\frac{n^2\pi^2}{L^2} - \sqrt{\frac{n^2\pi^2}{L^2}\frac{-N^b_{xx}}{D_b}}}. \tag{S29}$$

It follows that the solution for the middle layer takes the form

$$f_b = B_1\exp(\gamma_b y) + B_2\exp(-\gamma_b y) + B_3\exp(\beta_b y) + B_4\exp(-\beta_b y), \tag{S30}$$

where $\gamma_b = \sqrt{\frac{n^2\pi^2}{L^2} + \sqrt{\frac{n^2\pi^2}{L^2}\frac{-N^b_{xx}}{D_b}}}$ and $\beta_b = \sqrt{\frac{n^2\pi^2}{L^2} - \sqrt{\frac{n^2\pi^2}{L^2}\frac{-N^b_{xx}}{D_b}}}$.

4. if $\alpha_b = \alpha_a$, the roots of Eq. (S21) are

$$z = \pm\frac{n\pi}{L}, \qquad z = 0, \tag{S31}$$

for all the layers. It follows that the solution for the three layers takes the form

$$\begin{aligned} f_{a^+} &= A_1\exp(\gamma_a y)+A_2\exp(-\gamma_a y)+A_3 y\exp(\gamma_a y)+A_4 y\exp(-\gamma_a y),\\ f_{a^-} &= C_1\exp(\gamma_a y)+C_2\exp(-\gamma_a y)+C_3 y\exp(\gamma_a y)+C_4 y\exp(-\gamma_a y),\\ f_b &= B_1\exp(\gamma_b y)+B_2\exp(-\gamma_b y)+B_3 y\exp(\gamma_b y)+B_4 y\exp(-\gamma_b y). \end{aligned} \tag{S32}$$

where $\gamma_a=\gamma_b=\dfrac{n\pi}{L}$.

5. if $\dfrac{n^2\pi^2}{L^2}<-\dfrac{N^a_{xx}}{D_a}$ and $(\alpha_b<\alpha_a,\Delta T>0)$ or $(\alpha_b>\alpha_a,\Delta T<0)$, so that $N^a_{xx}<0, N^b_{xx}>0$, the roots of Eq. (S21) for the top and bottom layers are given by

$$z=\pm\sqrt{\frac{n^2\pi^2}{L^2}+\sqrt{\frac{n^2\pi^2}{L^2}\frac{-N^a_{xx}}{D_a}}}, z=\pm\sqrt{-\frac{n^2\pi^2}{L^2}+\sqrt{\frac{n^2\pi^2}{L^2}\frac{-N^a_{xx}}{D_a}}i}. \tag{S33}$$

It follows that the solution for the top and bottom layers takes the form

$$\begin{aligned} f_{a^+} &= A_1\exp(\gamma_a y)+A_2\exp(-\gamma_a y)+A_3\sin(\beta_a y)+A_4\cos(\beta_a y),\\ f_{a^-} &= C_1\exp(\gamma_a y)+C_2\exp(-\gamma_a y)+C_3\sin(\beta_a y)+C_4\cos(\beta_a y), \end{aligned} \tag{S34}$$

where $\gamma_a=\sqrt{\dfrac{n^2\pi^2}{L^2}+\sqrt{\dfrac{n^2\pi^2}{L^2}\dfrac{-N^a_{xx}}{D_a}}}$ and $\beta_a=\sqrt{-\dfrac{n^2\pi^2}{L^2}+\sqrt{\dfrac{n^2\pi^2}{L^2}\dfrac{-N^a_{xx}}{D_a}}}$.

Moreover, for the middle layer, the roots of Eq. (S21) are

$$z=\pm M\cos(\theta/2)\pm M\sin(\theta/2)i, \tag{S35}$$

where $M=\sqrt{\dfrac{n\pi}{L}\sqrt{\dfrac{n^2\pi^2}{L^2}+\dfrac{1}{D_b}N^b_{xx}}}$, and $\theta=\arctan\sqrt{\dfrac{N^b_{xx}L}{D_b n^2\pi^2}}$. Thus the solution for the middle layer is:

$$\begin{aligned} f_b &= B_1\exp(\gamma_b y)\sin(\beta_b y)+B_2\exp(\gamma_b y)\cos(\beta_b y)+\\ &\quad B_3\exp(-\gamma_b y)\sin(\beta_b y)+B_4\exp(-\gamma_b y)\cos(\beta_b y), \end{aligned} \tag{S36}$$

where $\gamma_b=M\cos(\theta/2), \beta_b=M\sin(\theta/2)$.

6. if $\dfrac{n^2\pi^2}{L^2}=-\dfrac{N^a_{xx}}{D_a}$ and $(\alpha_b<\alpha_a,\Delta T>0)$ or $(\alpha_b>\alpha_a,\Delta T<0)$, so that $N^a_{xx}<0, N^b_{xx}>0$, the solution for the middle layer is still given by Eq. (S36).

Differently, the roots of Eq. (S21) for the top and bottom layers are

$$z=\pm\frac{\sqrt{2}n\pi}{L}, \quad z=0. \tag{S37}$$

It follows that the solution for the top and bottom layers has the form:

$$\begin{aligned} f_1 &= A_1\exp(\gamma_a y)+A_2\exp(-\gamma_a y)+A_3+A_4 y,\\ f_3 &= C_1\exp(\gamma_a y)+C_2\exp(-\gamma_a y)+C_3+C_4 y, \end{aligned} \tag{S38}$$

where $\gamma_a=\dfrac{\sqrt{2}n\pi}{L}$.

7. if $\dfrac{n^2\pi^2}{L^2}>-\dfrac{N^a_{xx}}{D_a}$ and $(\alpha_b<\alpha_a,\Delta T>0)$ or $(\alpha_b>\alpha_a,\Delta T<0)$, so that $N^a_{xx}<0, N^b_{xx}>0$, the solution for the middle layer is still given by Eq. (S36).

Differently, the roots of Eq. (S21) for the top and bottom layers are

$$z=\pm\sqrt{\frac{n^2\pi^2}{L^2}+\sqrt{\frac{n^2\pi^2}{L^2}\frac{-N^a_{xx}}{D_a}}}, \quad z=\pm\sqrt{\frac{n^2\pi^2}{L^2}-\sqrt{\frac{n^2\pi^2}{L^2}\frac{-N^a_{xx}}{D_a}}} \tag{S39}$$

It follows that the solution for the top and bottom layers will have the form:

$$\begin{aligned} f_1 &= A_1 \exp(\gamma_a y) + A_2 \exp(-\gamma_a y) + A_3 \exp(\beta_a y) + A_4 \exp(-\beta_a y), \\ f_3 &= C_1 \exp(\gamma_a y) + C_2 \exp(-\gamma_a y) + C_3 \exp(\beta_a y) + C_4 \exp(-\beta_a y), \end{aligned} \tag{S40}$$

where $\gamma_a = \sqrt{\frac{n^2\pi^2}{L^2} + \sqrt{\frac{n^2\pi^2}{L^2}\frac{-N^a_{xx}}{D_a}}}$ and $\beta_a = \sqrt{\frac{n^2\pi^2}{L^2} - \sqrt{\frac{n^2\pi^2}{L^2}\frac{-N^a_{xx}}{D_a}}}$.

Having determined the form of the solution $f(y)$ in the three layers, the coefficients A_i, B_i and C_i appearing there are determined by imposing the boundary and continuity conditions (Eqs. (S22)). More specifically, we find that the boundary and continuity conditions are satisfied if

$$\mathbf{K}\mathbf{u} = \mathbf{0}, \tag{S41}$$

where $\mathbf{u} = [A_1, \cdots, A_4, B_1, \cdots, B_4, C_1, \cdots, C_4]^T$ and $\mathbf{K}$ is the 12×12 coefficient matrix. The critical value of swelling strain, $\varepsilon_{sw,cr} = \alpha \Delta T_{cr}$, is determined by equating to zero the determinant of $\mathbf{K}$.

FINITE ELEMENT SIMULATIONS

In this Section, we provide details about the Finite Element (FE) simulations conducted for this study using the commercial package Abaqus/Standard.

In all our numerical analysis, the material behavior of both elastomers is captured using a nearly incompressible hyperelastic Neo-Hookean model with initial shear moduli of $\mu_a = 3.6$ MPa and $\mu_b = 0.05$ MPa and extremely high bulk moduli, $K_a = 1000\mu_a$ and $K_b = 1000\mu_b$. This choice of μ and K results in a Poisson's ratio of 0.4995 for both materials, so that their initial Young's moduli are $E_a = 10.8$ MPa and $E_b = 0.15$ MPa. Moreover, to capture the swelling process we make a thermal analogy and assume that $\varepsilon_{sw} = \alpha\,\Delta T$, where α and ΔT denote the thermal expansion coefficient and temperature increase, respectively. In particular, we assume isotropic thermal expansion and choose $\alpha_a = 0.065$/K and $\alpha_b = 0.56$/K, so that $\alpha_a/\alpha_b = 0.116$ as measured in our experiments. Finally, although during swelling the Young's modulus of the materials is expected to decrease, for the sake of simplicity, we assume that $E_a/E_b = 72$ does not change.

All our simulations consist of two steps: (i) we first use a linear perturbation analysis (*BUCKLE module in Abaqus) to identify the critical buckling mode; (ii) we then introduce a small imperfection ($\approx 0.002L$) in the form of the critical mode into the mesh to guide the post-buckling analysis. It is important to note that in all our simulations the temperature is increased to simulate the immersion of the materials into a solvent.

Individual plate simulations. 3D models of the individual layered plates are constructed and discretized using 20-node quadratic brick continuum elements (Abaqus element type C3D20R). To allow rotation on the left and right surfaces, we fix u_x and u_z on the center line of the left surface and u_z on the center line of the right surface, while leaving u_x unset to enable expansion. Moreover, an *Equation constraint is applied to the center line of the right surface to ensure uniform u_x.

Unit cells simulations. To reduce the computational costs and make sure the response of the system is not dominated by boundary effects, we investigate the response of infinite 2D architected materials ad consider unit cells with periodic boundary conditions [2, 3]. 3D models of the unit cells shown in Fig. S6 are constructed and discretized into approximately 3000 elements using 20-node quadratic brick continuum elements (Abaqus element type C3D20R).

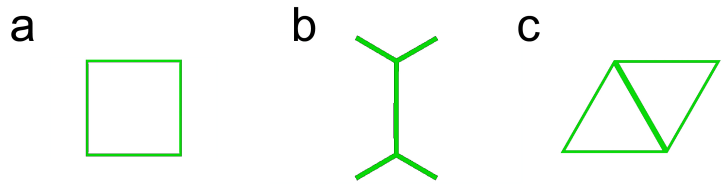

FIG. S6: Unit cells used in our simulations for (a) the square lattice, (b) the hexagonal lattice and (c) the triangular lattice.

Since upon swelling the infinite architected materials considered here can suddenly change their periodicity due to mechanical instability, we construct enlarged unit cells of various size and use a linear perturbation procedure to calculate their critical strains and corresponding modes. The critical strain of the infinite periodic structure is then defined as the minimum of the critical strains on all possible enlarged unit cells.

In Figs. S7a, S8a and S9a we report the critical strain for super cells consisting of $m \times n$ unit cells formed by plates #1 for the square, hexagonal and triangular lattice, respectively. The results indicate that the 2×2, 1×1 and 3×3 configurations have the minimum critical strain for the square, hexagonal and triangular lattice, respectively. Importantly, for both the square and hexagonal lattice the buckling pattern associated to the critical strain is characterized by all plates buckled into the first mode (an half sinusoidal), as shown in Figs. S7b and S8b.

Differently for the triangular lattice we find two modes associated to the critical strain (as shown in Fig. S9b): one "chiral" and one "symmetric".

Finally, non linear analyses are performed to capture the post-buckling behavior on enlarged unit cells with size dictated by the new periodicity introduced by buckling. In Fig. S10 we present the snapshots from the unit cell simulations for both the hexagon and triangle lattices. It's clear that only mode 1 buckling can be seen in hexagon lattice while a mixed mode 1 and 2 occurs in triangle lattice, as the "chiral" mode emerge in the postbuckling analysis.

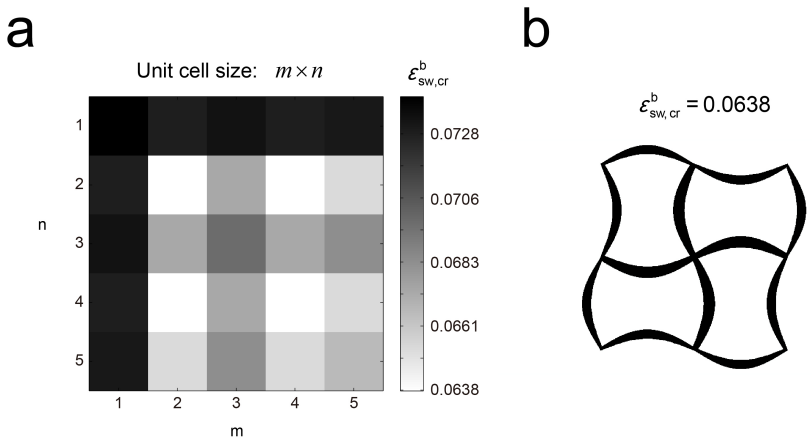

FIG. S7: (a) Critical strain for super cells consisting of $m \times n$ unit cells for the square lattice formed by plates #1. (b) Buckling pattern associated with the critical strain of the $2 \times n$ configuration.

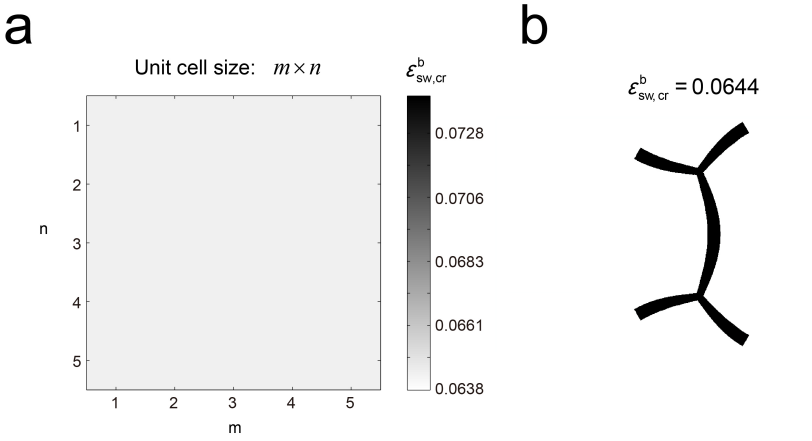

FIG. S8: (a) Critical strain for super cells consisting of $m \times n$ unit cells for the hexagonal lattice formed by plates #1. (b) Buckling pattern associated with the critical strain of the 1×1 configuration.

Finite size simulations To validate the unit cell simulations, we also performed finite size simulations on structures comprising an array of 10×10 cells. For this set of simulations 4 node rectangular reduced integration shell elements (Abaqus element type S4R) are used to reduce the computational cost. Moreover, all boundaries are assumed to be traction free.

In Fig. S11, we show several snapshots from the finite size simulation for the case in Fig. 3b. Clearly, the results support the unit size simulation and a periodic deformed pattern is seen.

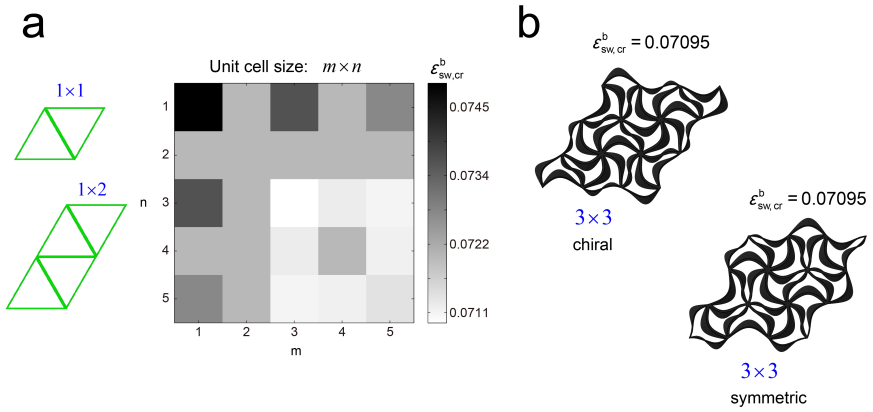

FIG. S9: (a) Critical strain for super cells consisting of $m \times n$ unit cells for the triangular lattice formed by plates #1. (b) Buckling patterns associated with the critical strain of the 3×3 configuration.

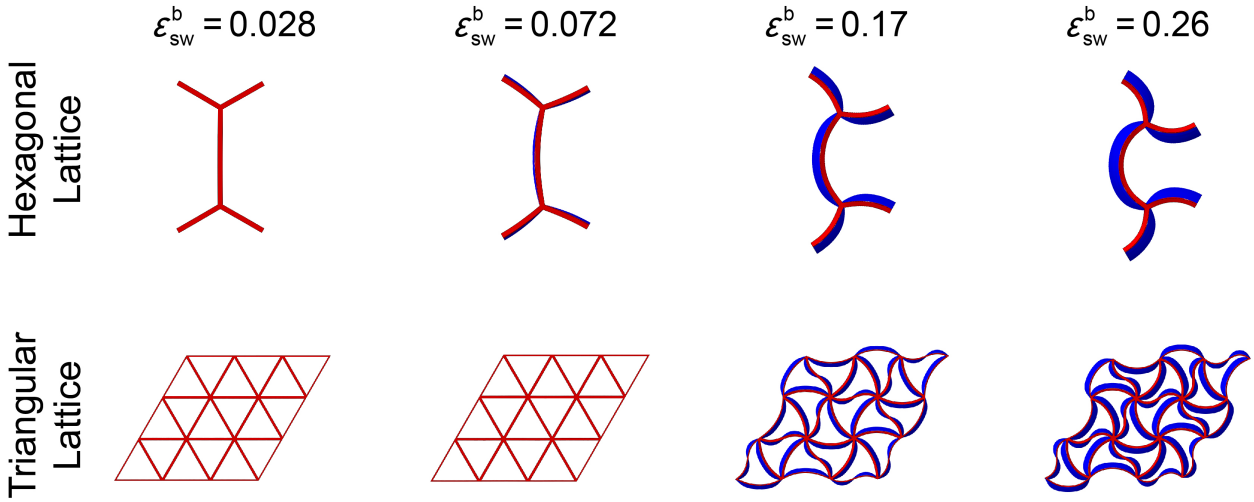

FIG. S10: Snapshots from the unit cell simulations for the hexagon (top) and triangle lattice (bottom).

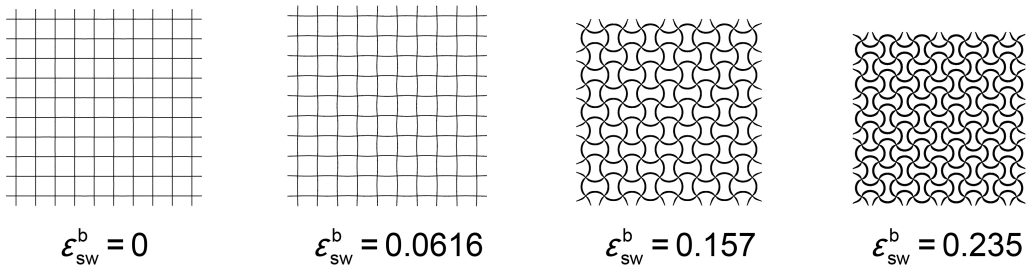

FIG. S11: Numerical snapshots during the swelling process for a square lattice made of plates #1.

[1] S. Timoshenko, S. Woinowsky-Krieger, and S. Woinowsky-Krieger, *Theory of plates and shells*, vol. 2 (McGraw-hill New York, 1959).
[2] K. Bertoldi, M. Boyce, S. Deschanel, S. Prange, and T. Mullin, Journal of the Mechanics and Physics of Solids **56**, 2642 (2008).
[3] M. Danielsson, D. Parks, and M. Boyce, Journal of the Mechanics and Physics of Solids **50**, 351 (2002).